ChemComm

FEATURE ARTICLE

View Article Online
View Journal | View Issue

Cite this: *Chem. Commun.*, 2023, **59**, 7875

Long-term heat-storage materials based on λ-Ti_3O_5 for green transformation (GX)

Shin-ichi Ohkoshi,*[a] Marie Yoshikiyo,*[a] Jessica MacDougall,[a] Yusuke Ikeda[a] and Hiroko Tokoro*[ab]

Received 12th February 2023,
Accepted 22nd May 2023

DOI: 10.1039/d3cc00641g

rsc.li/chemcomm

Effective reuse of waste heat energy is an important energy savings issue for green transformation. In general, phase-change heat storage materials cannot store energy for a prolonged period. If a solid material could conserve the accumulated thermal energy and release it only on demand, then its heat-storage application potential is considerably widened. From this angle, in 2015, we proposed the concept of a long-term heat-storage material, in which latent heat is preserved until the material is triggered by an external stimulus. This feature article describes long-term heat-storage ceramics composed of lambda-trititanium-pentoxide (λ-Ti_3O_5) from their discovery to heat-storage properties and future applications.

1. Proposal of long-term heat-storage materials for a green transformation

Climate change due to the rise of CO_2 concentration is a global problem. To safeguard our planet and pass it to the next generation of humanity, it is imperative to develop technologies and green innovation along with the accompanying social transformation, green transformation (GX).[1–14] Although producing nature-friendly energy (renewable energy) is vital, effective reuse of the produced energy and further energy savings are also important. From this point of view, we have developed eco-friendly materials (*i.e.*, heat-storage materials).[15,16] One material effectively reuses energy, while another is suitable for energy-conserving optical recordings.

For GX, reuse of waste heat energy is instrumental. Currently, approximately 40% of the consumed energy from sources such as oil, gas, and coal is released into the atmosphere as waste heat. This causes several negative

[a] *Department of Chemistry, School of Science, The University of Tokyo, 7-3-1 Hongo, Bunkyo-ku, Tokyo 113-0033, Japan. E-mail: ohkoshi@chem.s.u-tokyo.ac.jp, m-yoshikiyo@chem.s.u-tokyo.ac.jp*
[b] *Department of Materials Science, Faculty of Pure and Applied Sciences, University of Tsukuba, 1-1-1 Tennodai, Tsukuba, Ibaraki 305-8573, Japan. E-mail: tokoro@ims.tsukuba.ac.jp*

Shin-ichi Ohkoshi

Shin-ichi Ohkoshi is a Professor at the Department of Chemistry, School of Science, The University of Tokyo since 2006. He serves as the Project Officer of SPRING GX, JST, Director of the CNRS International Research Laboratory, Visiting Professor of the University of Manchester, and Honorary Member of Magdalen College, University of Oxford. Representatives awards he has received include the CSJ Award (2019) and Humboldt Research Award (2020). His research interests focus on functional phase transition materials based on metal oxides and metal complexes exhibiting light-induced phase transition, millimeter wave absorption, heat-storage properties, and so on. He has 550 publications and has submitted 300 patents.

Marie Yoshikiyo

Marie Yoshikiyo is an Assistant Professor at the Department of Chemistry, School of Science, the University of Tokyo. She received her BSc in 2011, MSc in 2013, and PhD in 2021 from the Department of Chemistry, School of Science, The University of Tokyo. She became Project Assistant Professor at the Department of Chemistry, School of Science, the University of Tokyo in 2015, and has started her current position in 2022. Her research interest mainly focuses on the development of functional metal oxides.

environmental effects.[7,8] Approximately 80% of this wasted heat energy is below 200 °C (473 K) (Fig. 1).[17] The development of high-performance heat-storage materials should help solve these problems. Known heat-storage materials include sensible ones such as bricks and concrete and solid–liquid latent heat-storage ones such as water, paraffin, and polyethylene glycol (Fig. 2).[10–15] In general, the heat energy accumulated in a heat-storage material is slowly released over time. The lack of long-term heat storage is known as the "time-gap problem." The ability to store heat long-term and release it on demand opens numerous practical applications.

Recently, we reported a new concept called long-term heat-storage ceramic.[15,16] A long-term heat-storage ceramic can conserve latent heat until the material is activated by an external stimulus. The material is lambda-trititanium-pentoxide (λ-Ti_3O_5), which shows a reversible phase transition to beta-trititanium-pentoxide (β-Ti_3O_5) by an external stimulus such as pressure. λ-Ti_3O_5 also exhibits a reversible photo-induced phase transition between β-Ti_3O_5 by light irradiation. Moreover, λ-Ti_3O_5 is a promising eco-friendly recording material composed of only common elements.

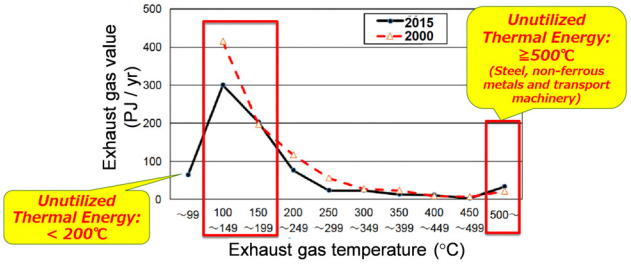

Fig. 1 Temperature range *vs.* the total amount of heat energy for the 38% of input resource energy wasted annually as heat in Japan. Of the wasted heat, 78% of the total caloric value is below 200 °C. Modified from figure in ref. 17, "Toward future utilization of unused heat" of the New Energy and Industrial Technology Development Organization (NEDO), Japan.

In this feature article, we describe λ-Ti_3O_5 and its metal-substituted series with potential as long-term heat-storage ceramics. This metal oxide can preserve the accumulated heat energy of the phase transition with β-Ti_3O_5. Applying external pressure releases the energy on demand. The rest of this article is organized as follows. Section 2 explains the discovery and basic physical properties of λ-Ti_3O_5. Section 3 describes the pressure-induced phase transition and heat-storage property. Section 4 demonstrates the control of the heat-storage property such as the necessary pressure for heat release and the heat-storage temperature. Section 5 discusses two other functionalities: light-induced and current-induced phase transitions. Finally, Section 6 provides the summary and future prospects.

Jessica MacDougall

Jessica MacDougall received her MChem from Durham University (UK) in 2017, and her MSc in chemistry from the University of Tokyo (Japan) in 2020. She is currently a PhD student in the solid-state physical chemistry laboratory of the Department of Chemistry, School of Science, the University of Tokyo under the supervision of Professor Shin-ichi Ohkoshi. Her research mainly focuses on functional metal oxide nanoparticles.

Yusuke Ikeda

Yusuke Ikeda received his bachelor degree in 2018 and master degree in 2020 from the Department of Chemistry, School of Science, the University of Tokyo. He is a PhD student at the Department of Chemistry, School of Science, the University of Tokyo under the supervision of Professor Shin-ichi Ohkoshi. His research interest mainly focuses on synthesis and investigation of the physical properties of functional materials based on metal complexes.

Hiroko Tokoro

Hiroko Tokoro has been a Professor of Materials Science at the University of Tsukuba since 2018. She received her BS from Keio University and ME from Kyoto University, followed by a PhD from the University of Tokyo and a JSPS postdoctoral fellowship (2004–2007). Her career includes working as a JST researcher (2007–2010), serving as an Assistant Professor at the University of Tokyo (2011–2013), and holding the position of Associate Professor at the University of Tsukuba (2013–2018). She has received several awards, including the CSJ Award for Young Scientist (2011), the German Innovation Award (2016), and the Yonezawa Memorial Prize of JPS (2020). Her research mainly focuses on bistability and phase transition in solid-state materials.

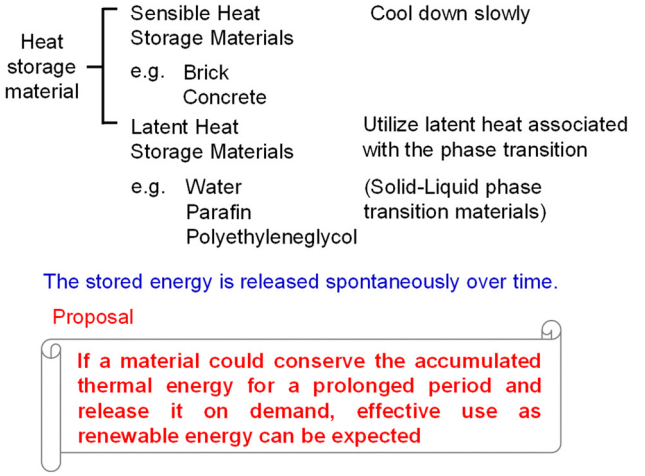

Fig. 2 Classifications and common examples of current short-term heat-storage materials.

2. Discovery of λ-Ti_3O_5 and its physical properties

Titanium oxide, TiO_2, is a common metal oxide. Tetravalent TiO_2 is white. It is used as a white pigment for cosmetics or buildings and as a photocatalyst. By contrast, other titanium oxides, including trivalent titanium, show a black color. They are used in black-color cosmetics or as heat-absorbing materials (Fig. 3). The black color originates from the d-electron in the trivalent titanium. Combining the trivalent and tetravalent titanium ions generates various titanium oxides (TiO_2, Ti_4O_7, Ti_3O_5, Ti_2O_3, *etc.*), which display a range of colors from white to pitch black.

To discover new materials or functionalities, we investigated titanium oxide nanoparticles. Nanoparticles of white titanium oxide (TiO_2) have been intensively studied for various applications such as photocatalysts. Despite their interesting features, nanoparticles of black titanium oxides are less studied. For example, single crystal of Ti_3O_5 exhibits a metal–insulator phase transition or an antiferromagnetic transition.[18] Our research focuses on nanoparticle synthesis of Ti_3O_5 to elucidate the influence of particle size on the phase transition properties.[15,16,19,20]

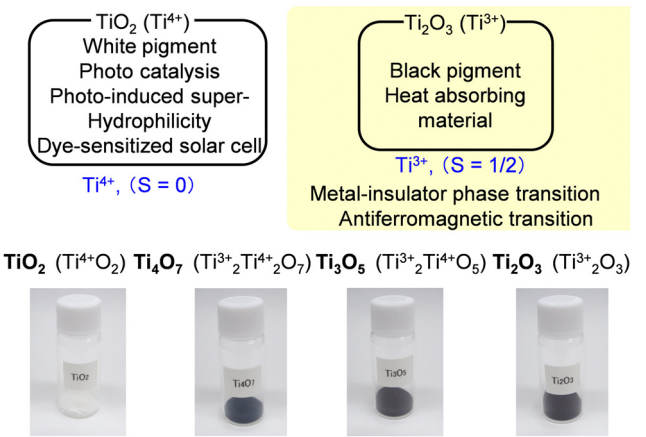

Fig. 3 Appearance, properties, and valence states of known titanium oxides.

Synthesis and morphology of λ-Ti_3O_5

We initially synthesized Ti_3O_5 as nanoparticles by the following process.[15] First, nanoparticles were trapped in glass by a combination method of reverse-micelle and sol–gel processes. Then the precursor was sintered under a hydrogen flow to obtain titanium oxide nanoparticles in the glass matrix. Fig. 4(a) shows the transmission electron microscopy (TEM) image of the obtained nanoparticles in the glass matrix. Finally, the glass matrix was chemically etched to obtain the nanoparticles (Fig. 4(a), inset). The powder X-ray diffraction (PXRD) pattern indicated a new monoclinic structure (space group $C2/m$) (Fig. 4(b) and (c)). We discovered this new type of titanium oxide in 2010 and named it "lambda-trititanium-pentoxide (λ-Ti_3O_5)".

λ-Ti_3O_5 shows several types of morphologies, depending on the synthesis. The aforementioned initial synthesis of λ-Ti_3O_5 gave nanocrystals in a SiO_2 matrix. The sol–gel method also produces λ-Ti_3O_5 nanocrystals.[19] The sintering temperature can control the size of the nanocrystals: 8 ± 2 nm for 1123 °C, 9 ± 3 nm for 1133 °C, 9 ± 2 nm for 1143 °C, 10 ± 3 nm for 1153 °C, 11 ± 4 nm for 1163 °C, 13 ± 4 nm for 1173 °C, 25 ± 12 nm for 1200 °C, and 36 ± 15 nm for 1250 °C.

Another synthesis method to prepare large batches of λ-Ti_3O_5 in fewer steps is to simply sinter anatase-TiO_2 nanoparticles (size = 7 nm) under a hydrogen flow.[15] Fig. 5(a) (upper) shows the scanning electron microscopy (SEM) image of the obtained sample, which has a coral-like morphology with a particle size of 2 μm. Fig. 5(a) (lower) shows the TEM image,

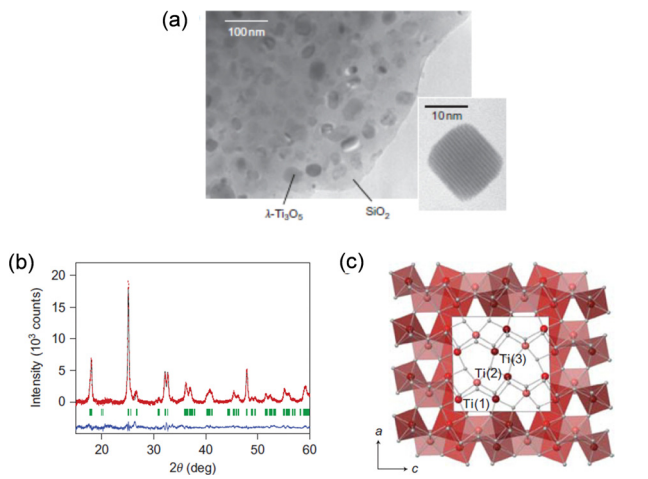

Fig. 4 (a) TEM image of λ-Ti_3O_5 nanoparticles embedded in the SiO_2 matrix. Inset shows a single nanocrystal. (b) PXRD pattern of λ-Ti_3O_5 in SiO_2 with Rietveld analysis. Red dots, black lines, and blue lines show the observed pattern, calculated pattern, and their difference, respectively. Green bars show the calculated Bragg positions of λ-Ti_3O_5. (c) Crystal structure of monoclinic λ-Ti_3O_5. Reproduced from ref. 15, copyright 2010 Springer Nature.

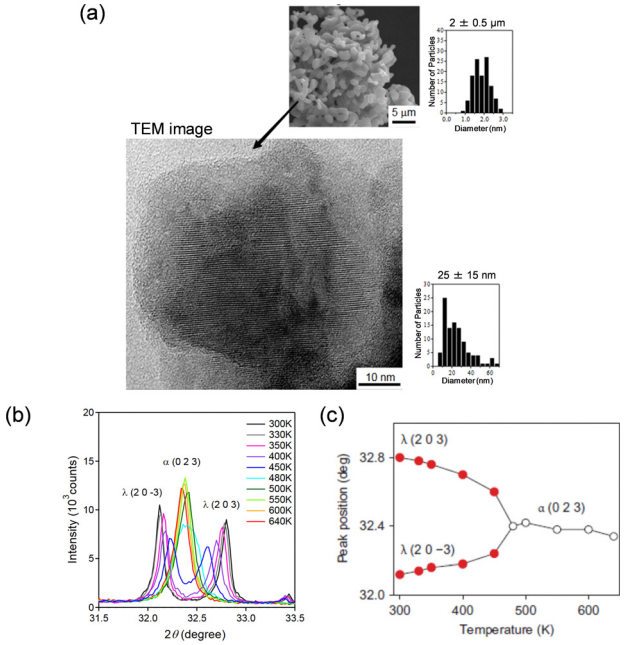

Fig. 5 (a) HRTEM image of λ-Ti_3O_5 prepared from anatase-TiO_2 and its nanocrystal size distribution. Inset shows the SEM image and the size distribution of flake-form λ-Ti_3O_5. (b) Temperature dependence of the PXRD pattern between 31.5° and 33.5°. (c) Temperature dependence of the (2 0 3) peak of λ-Ti_3O_5 and (0 2 3) peak of α-Ti_3O_5. Reproduced from ref. 15, copyright 2010 Springer Nature.

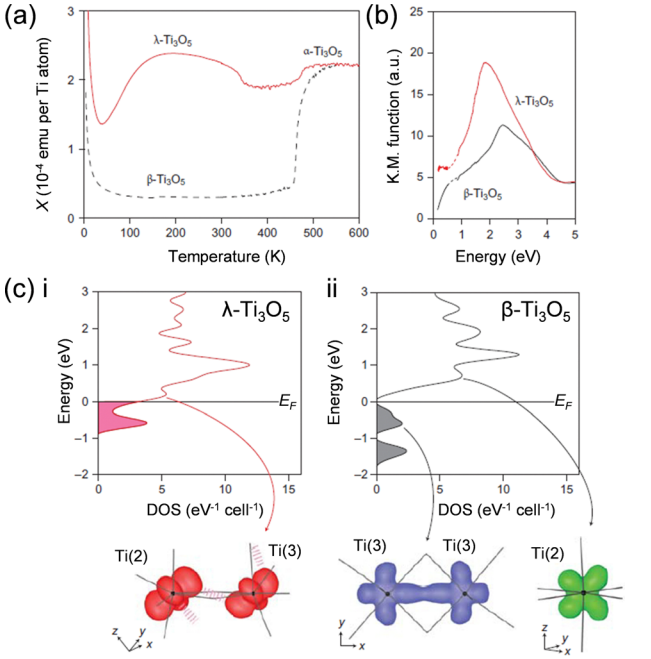

Fig. 6 (a) χ *vs.* T at 0.5 T for flake-form λ-Ti_3O_5 (red) and single-crystal β-Ti_3O_5 (dashed black). (b) UV-vis and IR absorption spectra for flake-form λ-Ti_3O_5 (red) and single-crystal β-Ti_3O_5 (dashed black). (c) Band structures calculated by VASP for (i) λ-Ti_3O_5 and (ii) β-Ti_3O_5 with electron-density maps for the Fermi level displayed below. Reproduced from ref. 15, copyright 2010 Springer Nature.

indicating that the flake-form morphology is an assembly of primary nanocrystals with an average particle size of 25 nm. This approach can yield λ-Ti_3O_5 in large quantities.

PXRD measurements acquired as the temperature is increased show that the diffraction peaks of λ-Ti_3O_5 are converted to α-Ti_3O_5 peaks continuously, for example (2 0 −3) and (2 0 3) of λ-Ti_3O_5 → (0 2 3) of α-Ti_3O_5 (Fig. 5(b) and (c)). Furthermore, heating the sample to 640 K and subsequently cooling it to 300 K causes α-Ti_3O_5 peaks to return to λ-Ti_3O_5 peaks.

Magnetic and electric properties

Fig. 6(a) shows the magnetic susceptibility (χ) *versus* temperature (T) curve of the flake-form λ-Ti_3O_5 and that of a conventional single-crystal β-Ti_3O_5. The χ value of λ-Ti_3O_5 across the measured temperature range remains at *ca.* 2×10^{-4} emu per Ti atom, suggesting that λ-Ti_3O_5 is a Pauli paramagnet due to metallic conduction. The estimated electrical conductivity (σ) value for λ-Ti_3O_5 is 30 S cm^{-1}, indicating that it is a near metallic conductor. This is consistent with the magnetic data. Fig. 6(b) shows the ultraviolet-visible (UV-vis) and infrared (IR) reflectance spectra. λ-Ti_3O_5 exhibits metallic absorption over these wavelength ranges. By contrast, β-Ti_3O_5 is a semiconductor with a band gap of 0.14 eV and a calculated conductivity of 3×10^{-2} S cm^{-1}.

The valence states for the three Ti sites in λ-Ti_3O_5 were estimated using the link between the valence state and the bond length.[21] The calculated valence states for Ti(1), Ti(2), and Ti(3) are +3.37, +3.20, and +3.53, respectively. These values are close to that of $Ti^{(10/3)+}$, suggesting that the charge is delocalized over the structure. This further supports that λ-Ti_3O_5 is a metallic conductor. By contrast, the valence states of β-Ti_3O_5 suggest that it has a charge-localized system of Ti^{3+}–$Ti^{(11/3)+}$–$Ti^{(10/3)+}$ as the valence states of Ti(1), Ti(2), and Ti(3) in β-Ti_3O_5 are +3.00, +3.79, and +3.32, respectively.

First-principles calculations for λ-Ti_3O_5 indicate that the bands residing close to the Fermi level are the t_{2g} orbitals from the Ti ion octahedral 3d orbitals. These are split by coupling with adjacent Ti ions. The d_{xy} orbital on Ti(2) forms slipped π stacking (akin to a zig-zag chain) with the d_{xy} orbital on Ti(3), which is located at the Fermi level (Fig. 6(c), left), making λ-Ti_3O_5 a metallic conductor. In semi-conducting β-Ti_3O_5, the valence band at −0.60 eV consists of a bipolaron of Ti(3)–Ti(3) formed by σ-bonding with the d_{xy} orbitals on Ti(3). The conduction band at +0.71 eV mainly consists of a vacant d_{xz} orbital on Ti(2) (Fig. 6(c), right).

3. Pressure-induced phase transition and heat-storage properties of λ-Ti_3O_5

Material and morphology

The heat-storage properties and the pressure-induced phase transition were investigated using λ-Ti_3O_5 samples synthesized using rutile-TiO_2 particles as the starting material.[16] Rutile-TiO_2 has a particle size of *ca.* 500 nm, which is much larger than

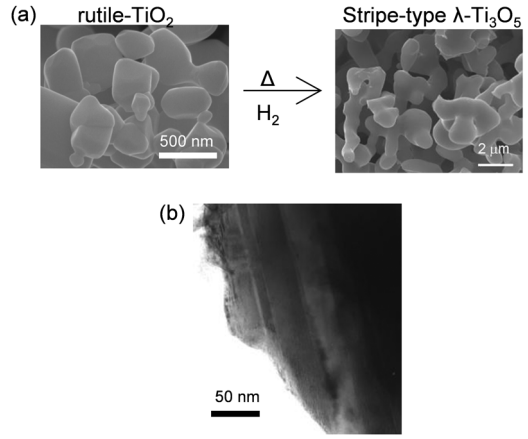

Fig. 7 (a) SEM images of (i) rutile-TiO_2 and (ii) stripe-type λ-Ti_3O_5. (b) TEM image of stripe-type λ-Ti_3O_5 showing 200 nm × 30 nm stripe-type crystal domains. Reproduced from ref. 16, copyright 2015 Springer Nature.

anatase-TiO_2 (Fig. 7, upper left). The obtained sample shows a coral-like morphology composed of rectangular-shaped nanorods measuring 200 nm × 30 nm, which we refer to as stripe-type λ-Ti_3O_5.

Pressure-induced phase transition

The pressure (P) dependence of the crystal structure of stripe-type λ-Ti_3O_5 was measured by PXRD. Fig. 8(a) shows the PXRD pattern of the sample at 300 K under atmospheric pressure (P = 0.1 MPa). Rietveld analysis indicated that the sample is 80% λ-Ti_3O_5 and 20% β-Ti_3O_5. By applying P = 510 MPa, the PXRD pattern changes to that of β-Ti_3O_5 (Fig. 8(b)). Fig. 8(c) shows the pressure dependence of the phase fractions of λ-Ti_3O_5 and β-Ti_3O_5. The pressure where the fraction of λ-Ti_3O_5 becomes 50% ($P_{1/2}$) is ~60 MPa. Upon further heating, the pressure-formed β-Ti_3O_5 returns to λ-Ti_3O_5 at 470 K (Fig. 8(d)).

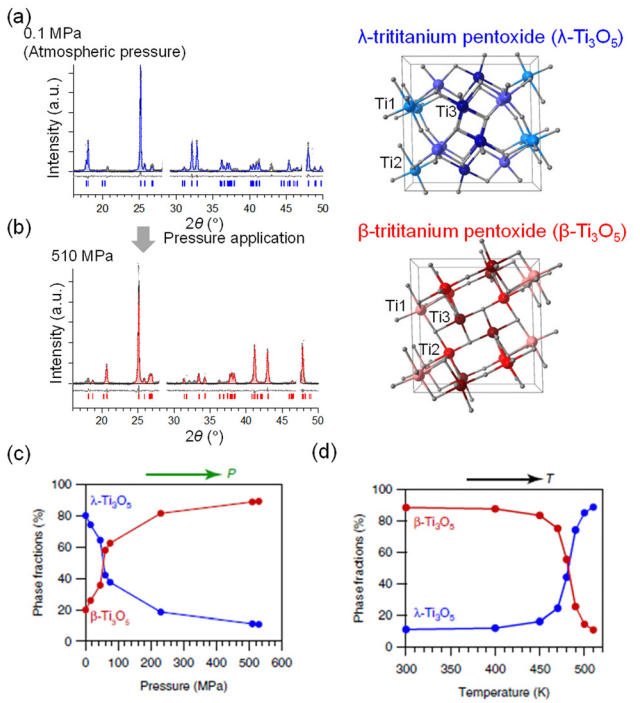

Fig. 8 (a) PXRD pattern of stripe-type λ-Ti_3O_5 at ambient pressure. (b) PXRD of β-Ti_3O_5 after applying 510 MPa pressure. (c) Pressure dependence of the phase fractions of λ-Ti_3O_5 and β-Ti_3O_5. (d) Temperature dependence of the phase fractions of λ-Ti_3O_5 and β-Ti_3O_5. Reproduced from ref. 16, copyright 2015 Springer Nature.

Accumulated heat energy and pressure-released energy

Differential scanning calorimetry (DSC) was performed for a detailed examination of the heat-storage process. The transition enthalpy (ΔH) for the first-order phase transition of β-Ti_3O_5 to λ-Ti_3O_5 is 230 ± 20 kJ L^{-1} (12 ± 1 kJ mol^{-1}) (Fig. 9(a)). During the DSC measurement as the temperature decreased, a peak did not appear, indicating that the system conserves the accumulated heat energy of the phase transition from β-Ti_3O_5 to λ-Ti_3O_5.

To measure the amount of energy released, pressure was applied to the sample to induce a phase transition of stripe-type λ-Ti_3O_5 to β-Ti_3O_5. The released heat energy is 240 ± 40 kJ L^{-1}, which is almost the same as the heat accumulated energy (Fig. 9(b)). The DSC curves show that this material conserves the heat energy of the first phase transition of β-Ti_3O_5 to λ-Ti_3O_5. However, this stored energy is released when a low pressure is applied to induce the reverse phase transition of λ-Ti_3O_5 to β-Ti_3O_5.

Mechanism

First-principles phonon-mode calculations were conducted for a deeper understanding of the pressure-induced phase transition. Fig. 10(a) shows the calculated phonon density of states (phonon DOS) for λ-Ti_3O_5 and β-Ti_3O_5. During the pressure-induced phase transition of λ-Ti_3O_5 to β-Ti_3O_5, the coordination geometry of Ti(3) changes. The Ti(3)–O(4) bond forms as the Ti(3)–O(5) bond breaks. The significant phonon modes of λ-Ti_3O_5 to this transition appear at 248.6 cm^{-1}, 318.5 cm^{-1}, and 445.8 cm^{-1}. In the B_u phonon mode at 445.8 cm^{-1}, Ti(3) vibrates away from O(5) and towards O(4) (Fig. 10(b), upper). During the reverse phase transition (thermally induced), where the Ti(3)–O(4) bond is broken and the Ti(3)–O(5) bond is reformed, the significant phonon modes are 226.7 cm^{-1} and

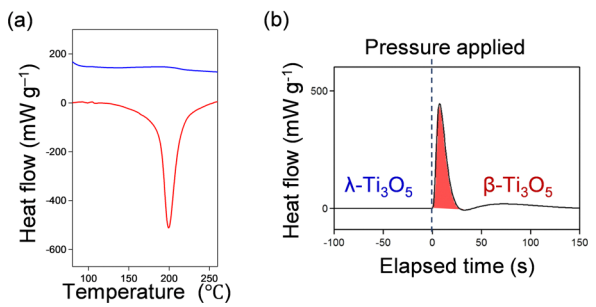

Fig. 9 DSC measurements showing (a) the heat-induced transition of β-Ti_3O_5 to λ-Ti_3O_5 and (b) the pressure-induced phase transition of stripe-type λ-Ti_3O_5 to β-Ti_3O_5. Reproduced from ref. 16, copyright 2015 Springer Nature.

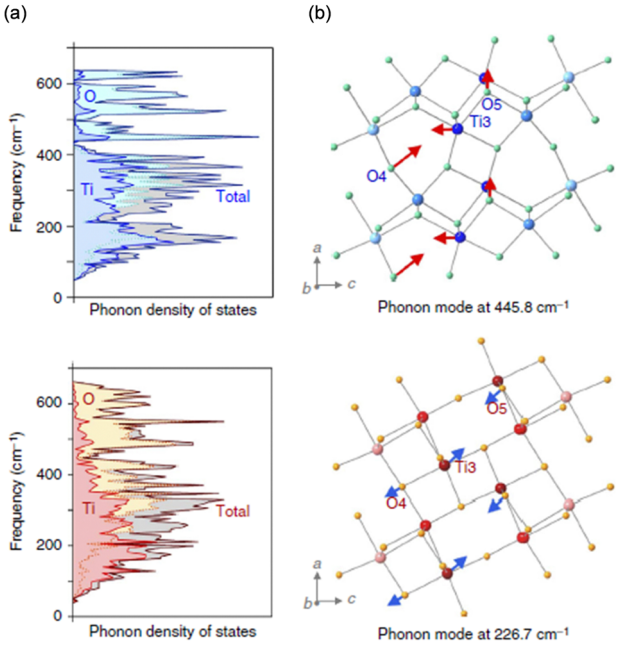

Fig. 10 (a) Phonon DOS for stripe-type λ-Ti_3O_5 (upper) and β-Ti_3O_5 (lower). (b) Visualizations of the B_u phonon mode for stripe-type λ-Ti_3O_5 (upper) and β-Ti_3O_5 (lower). Reproduced from ref. 16, copyright 2015 Springer Nature.

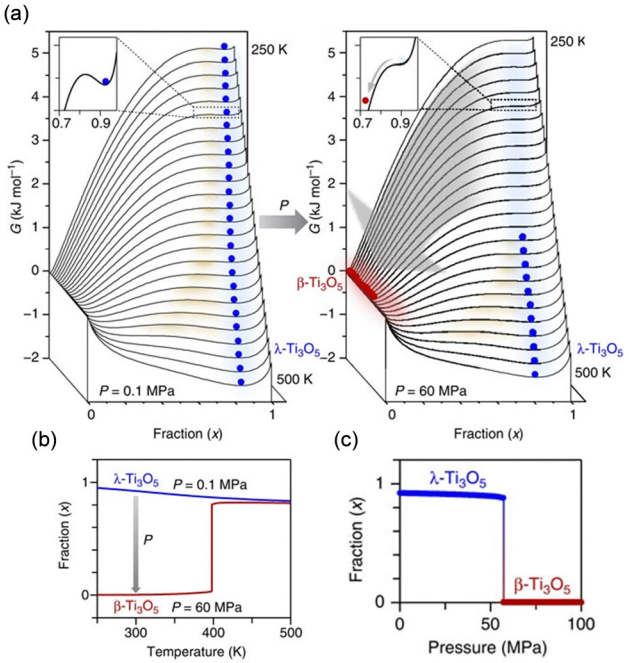

Fig. 11 (a) Gibbs free energy (*G*) *vs.* fraction of λ-Ti_3O_5 (*x*) calculated by the Slichter–Drickamer mean-field model at (i) 0.1 MPa and (ii) 60 MPa external pressure. Blue and red circles denote λ-Ti_3O_5 and β-Ti_3O_5, respectively. (b) *x vs. T* curves at 0.1 MPa (blue) and 60 MPa (red) external pressures. (c) *x vs.* pressure curve at 300 K. Reproduced from ref. 16, copyright 2015 Springer Nature.

339.3 cm^{-1}. In the B_u phonon mode at 226.7 cm^{-1}, Ti(3) now vibrates away from O(4) towards O(5) (Fig. 10(b), lower).

The Slichter and Drickamer mean field model[22] was deployed to elucidate the thermodynamics of the pressure-induced phase transition from λ-Ti_3O_5 to β-Ti_3O_5. In this model, *G* is defined by the transition enthalpy (ΔH), the transition entropy (ΔS), and an interaction parameter between the λ-Ti_3O_5 and β-Ti_3O_5 phases. The change in Gibbs free energy (*G*) dictates the generation of stripe-type λ-Ti_3O_5 *vs.* β-Ti_3O_5, and this change is thought to occur at the surface/interfacial energy of the nanoscale domain. Fig. 11(a) shows the *G vs.* λ-Ti_3O_5 fraction (*x*) curves from this calculation. Under atmospheric pressure (P = 0.1 MPa), the sample is stable as λ-Ti_3O_5 after it is formed at higher temperatures due to the energy barrier for the transition between λ-Ti_3O_5 and β-Ti_3O_5. When external pressure is applied, the *G vs. x* curves are affected. Because no energy barrier is present below 400 K for P = 60 MPa, there is a pressure-induced phase transformation from λ-Ti_3O_5 to β-Ti_3O_5. Fig. 11(b) plots the *x vs.* temperature curves for P = 0.1 MPa and P = 60 MPa, and Fig. 11(c) shows the *x vs.* pressure curve at 300 K, which represents the threshold of this pressure-induced transition.

In the SD model, this pressure-induced phase transition originates from the $P\Delta V$ term of the enthalpy change ($\Delta H = \Delta U + P\Delta V$). From the phonon-mode calculations, the pressure-induced change of $P\Delta V$ at 60 MPa is 0.19 kJ mol^{-1}, which is two orders of magnitude larger than the change in internal energy (ΔU) of 1×10^{-3} kJ mol^{-1}. The effect on ΔS is also negligible and does not significantly contribute to the phase transition.

In developing novel heat-storage materials, structural phase transition materials have potential as heat-storage materials. In addition to the sufficient magnitude of transition enthalpy, an important criterion for a heat-storage material is to possess a thermal hysteresis in the phase transition. The larger the hysteresis, the wider the possible temperature range is for heat-storage. In the case of λ-Ti_3O_5, the thermal hysteresis is so wide that this phase is maintained through all temperatures below the heat-storage temperature.[15,16] This is the unique characteristic of λ-Ti_3O_5 realizing the "long-term" heat-storage ceramic that does not release the accumulated heat unless stimulated by pressure. λ-Ti_3O_5 and its metal-substituted series are the only "long-term" heat-storage materials up to date.

4. Tuning the heat-storage properties of λ-Ti_3O_5

Controlling the necessary pressure for heat release

Vehicles (*e.g.*, cars, trucks, and buses) use heat energy from combusting fuel in an engine to gain power. The realization of technologies that can store and reuse waste heat while driving would drastically improve fuel consumption. For such applications, the necessary pressure for heat release must be low to compactly equip the heat-release system in an automobile. We investigated the effect of sintering conditions during the synthesis on the necessary pressure for heat release.[23]

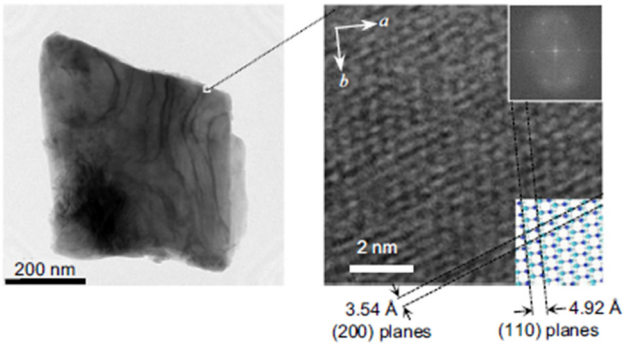

Fig. 12 TEM image of block-type λ-Ti_3O_5 (left) with an enlarged image showing clear lattice fringes (right). Inset shows the FFT image (upper) and the corresponding lattices (lower). Reproduced from ref. 23, copyright 2019 Springer Nature.

The sample was prepared by 1300 °C sintering of rutile-type TiO_2 under a hydrogen gas flow. Rietveld analysis of the PXRD pattern determined that λ-Ti_3O_5 has a monoclinic structure with a *C*2/*m* space group. The sample is comprised of block-shaped crystals (Fig. 12). The crystal size is in the sub-micrometer range, which is notably larger than the previously reported samples (stripe-type λ-Ti_3O_5). This material is called block-type lambda-trititanium-pentoxide (block-type λ-Ti_3O_5), which reflects the primary particle morphology.

PXRD patterns were measured at different applied external pressures to investigate the pressure effect on block-type λ-Ti_3O_5 (Fig. 13(a) and (b)). As *P* increases, the phase fraction of λ-Ti_3O_5 decreases, whereas that of β-Ti_3O_5 increases until 30 MPa. Above 30 MPa, the phase fractions remain constant. The $P_{1/2}$ value is 7 MPa.

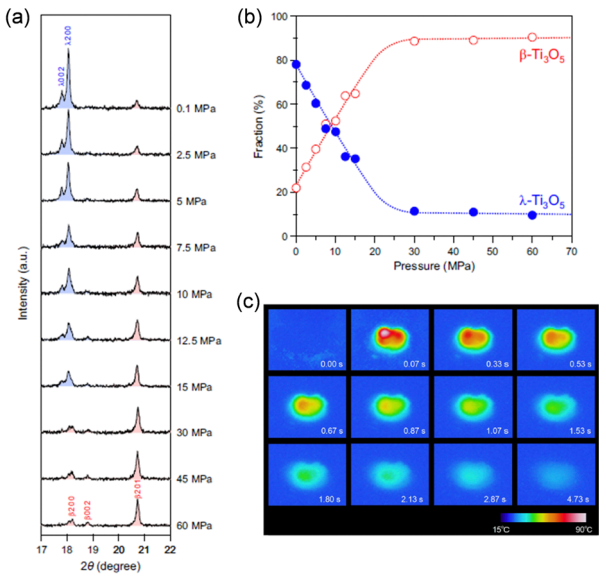

Fig. 13 (a) Pressure-dependent PXRD patterns from 0.1 to 60 MPa external pressures. (b) Phase fraction *vs.* pressure curves of block type λ-Ti_3O_5 (blue) and β-Ti_3O_5 (red). (c) Thermographic images of block-type λ-Ti_3O_5 after applying external pressure at *t* = 0. Reproduced from ref. 23, copyright 2019 Springer Nature.

Thermography was employed to visually measure the temperature change during a pressure-induced phase transition induced by striking the sample with a hammer. The initial thermal image is blue, and the starting temperature is 26.8 °C. After striking the sample, the thermal image changes to white, and then progressively turns red, orange, yellow, green, and finally returns to blue (Fig. 13(c)). The maximum temperature of the white area is 85.5 °C, which is reached less than 67 ms after applying pressure. These results demonstrate that the heat energy is released immediately upon applying pressure and the temperature exponentially decreases over time with a decay time of 1.7 s.

Materials for use in vehicles should have transition pressures below 10 MPa. Hence, this current heat-storage ceramic has potential for applications in automobile components near engines or mufflers, as the heat-storage ceramic can be employed to rewarm cooled internal systems when the vehicle is restarted. Additionally, changing the morphology can control the threshold pressure.

Controlling the heat-storage temperature

Another important property is the heat-storage temperature. λ-Ti_3O_5 stores heat near 200 °C and undergoes a phase transition from β-Ti_3O_5 to λ-Ti_3O_5. If the heat-storage temperature can be controlled and lowered, the potential for development as heat-storage materials will greatly expand. Thus, the effect of replacing titanium ions with other metal ions has been examined.

The synthesis of magnesium-substituted λ-Ti_3O_5 was first reported by our group in 2017.[24] Subsequently, in 2019, Wang *et al.* discovered that with Mg-substitution, the phase-transition temperature of λ-Ti_3O_5 to α-Ti_3O_5 to is decreased.[25] We then investigated the effect on the pressure-induced phase transition of λ-Ti_3O_5 to β-Ti_3O_5 in 2022.[26]

Mg-substituted λ-Ti_3O_5 (λ-$Mg_xTi_{3-x}O_5$) was synthesized using the following procedure (Fig. 14(a)). First, an aqueous ammonia solution was added to a mixed dispersion of rutile TiO_2 particles in aqueous magnesium acetate, forming the Mg ion-covered TiO_2 precursor. This precursor was sintered at 1300 °C under a hydrogen gas flow to give λ-$Mg_xTi_{3-x}O_5$ (x = 0.015, 0.022, 0.043, and 0.053). SEM images showed that the samples have a coral-like shape. Increasing the Mg substitution gradually reduces the diameter of the coral-like structure (Fig. 14(b)). The diameter at x = 0.053 is about half that at x = 0.015.

The heat-storage properties were evaluated by DSC measurements. The DSC curves contain endothermic peaks at heat-storage temperatures of 178 °C (x = 0.015), 160 °C (x = 0.022), 108 °C (x = 0.043), and 80 °C (x = 0.053) (Fig. 14(c)). The transition enthalpy values are 227 kJ L^{-1} (x = 0.015), 223 kJ L^{-1} (x = 0.022), 215 kJ L^{-1} (x = 0.043), and 216 kJ L^{-1} (x = 0.053) (Fig. 14(d)). Mg cation substitution decreases the heat-storage temperature from 198 °C (x = 0) to 80 °C (x = 0.053), while maintaining the accumulated heat energy. This reduced heat-storage temperature can be understood by the narrowing of the thermal hysteresis loop caused by the decrease of the interaction parameter within the crystal due to defects, which is

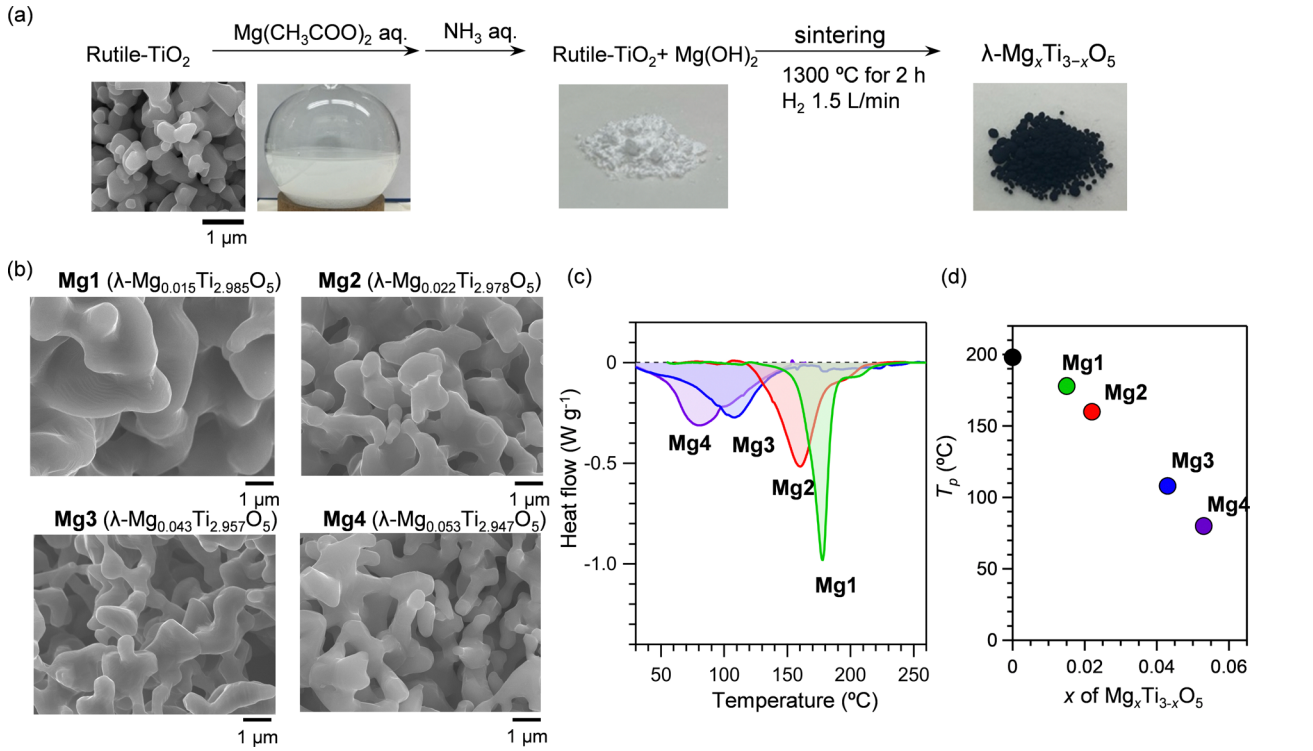

Fig. 14 (a) Synthesis procedure of Mg-substituted λ-Ti_3O_5 (b) SEM images of λ-$Mg_xTi_{3-x}O_5$ with a coral-like morphology. (c) DSC measurements of Mg-substituted λ-Ti_3O_5 samples. (d) *x vs. T* dependence on the transition temperature. Reproduced from ref. 26, with permission from the Royal Society of Chemistry.

supported by mean-field thermodynamic simulations proposed by Slichter and Drickamer (the SD model).

Furthermore, an Sr-substituted λ-Ti_3O_5 (λ-$Sr_xTi_{3-x}O_5$) was synthesized.[27] λ-$Sr_xTi_{3-x}O_5$ shows an endothermic peak at 67 °C (340 K) during the DSC measurement, which is below the boiling temperature of water (100 °C). Sc substitution can effectively reduce the heat-storage temperature of the heat-storage ceramics. First-principles calculations suggest that the decrease of the heat-storage temperature (= $\Delta H/\Delta S$) originates from the decrease in the ΔH value caused by Sc substitution.

As summarized in Fig. 15, the present long-term heat-storage property in λ-Ti_3O_5 provides insight into a new concept called heat-storage ceramics. Heat-storage ceramics can store heat energy for a prolonged period as latent heat and release this stored energy on demand by a pressure application. Furthermore, metal substitution on λ-Ti_3O_5 is an effective approach to broaden the heat-storage performance.

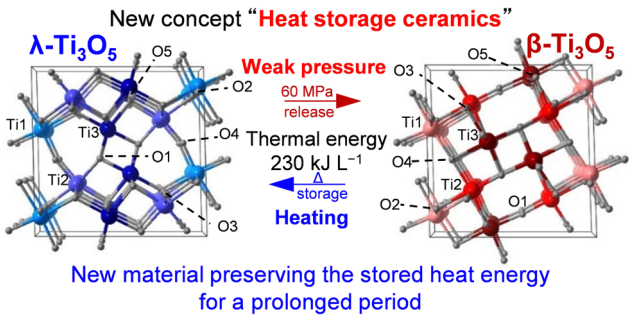

Fig. 15 Concept of "heat-storage ceramics" showing an external stimulation-induced reversible phase transfer between λ-Ti_3O_5 (left) and β-Ti_3O_5 (right).

As a future direction for the development of long-term heat-storage materials, controlling the thermal hysteresis is the key. Any first-order phase transition material with a thermal hysteresis can be a candidate for latent heat-storage materials, and the width of the thermal hysteresis decides the active temperature range and the energy storage period. A previous study indicates that the interaction parameter, which is affected by the crystalline size, defects, *etc.*, influences the width of the thermal hysteresis.[23,26,28] Exploring the hysteresis of various first-order phase transitions could lead to the discovery of new families of long-term heat-storage materials.

5. Other functions: light- and current-induced phase transitions

Light-induced phase transition

Herein we introduce a metal–semiconductor phase transition with λ-Ti_3O_5 at ambient temperature.[15] This was the first demonstration of a photo-rewritable phenomenon for a metal oxide. This phenomenon is possible due to the specific state of λ-Ti_3O_5, which is trapped at a thermodynamic local energy minimum.

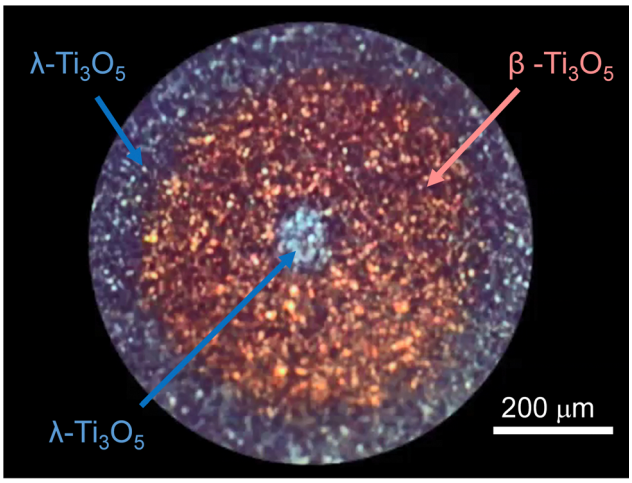

Fig. 16 Photograph showing the result of irradiating flake-form λ-Ti_3O_5 with a 532 nm nanosecond laser pulse followed by a 410 nm nanosecond laser pulse.

Irradiating the flake form of λ-Ti_3O_5 with 532 nm nanosecond laser light (6 ns, five shots, 1.5×10^{-5} mJ μm^{-2} $pulse^{-1}$) at room temperature causes the irradiated area to change from navy to brown. Further irradiating with 410 nm laser light (8×10^{-3} mW μm^{-2}) restores the navy color at the irradiated spot (Fig. 16). The color change by alternating light irradiation with 532 nm and 410 nm light is repeatedly observed. The XRD pattern indicated that the brown area is β-Ti_3O_5. Irradiating with 532 nm light induces a phase transition from λ-Ti_3O_5 to β-Ti_3O_5, as demonstrated by the color change of navy to brown. By contrast, irradiating with 410 nm light induces the reverse transition. A similar phase-transition pattern appears when the sample is irradiated with 355 and 1064 nm nanosecond-pulsed laser light.

The SD model can explain the mechanism of the light-induced phase transition. As explained in Section 3, an energy barrier exists between the charge-localized β-Ti_3O_5 and charge-delocalized λ-Ti_3O_5 throughout the entire temperature range when an external pressure is not applied. The light-induced phase transition from λ-Ti_3O_5 (navy) to β-Ti_3O_5 (brown) is a transition from a thermodynamically trapped metastable phase at a local energy minimum state to the true stable phase by light. Since metallic absorption allows λ-Ti_3O_5 to effectively absorb light over a wide range of wavelengths from ultraviolet to near-infrared, the λ- to β-Ti_3O_5 transition appears by irradiating with 355, 532, or 1064 nm nanosecond-pulsed laser lights. The reverse photo-induced phase transition from β-Ti_3O_5 to λ-Ti_3O_5 is an excitation from the valence band to the conduction band on β-Ti_3O_5, where the excited state changes directly to λ-Ti_3O_5 in the pulsed laser irradiation or as a photothermal transition from β-Ti_3O_5 to λ-Ti_3O_5.

Recently, dynamic observations of the light-induced phase transition from β-Ti_3O_5 to λ-Ti_3O_5 were performed using ultrafast time-resolved PXRD measurements at the Swiss X-ray Free Electron Laser facility (Swiss-FEL).[29] The experiments revealed that the crystal structure of the Ti_3O_5 crystal deforms within 500 fs after light irradiation and the phase transition is proceeded by strain waves propagating from the light-irradiated Ti_3O_5 surface through the crystal on the order of picoseconds (Fig. 17). This propagation speed is much faster than the phase transition caused by thermal diffusion (*ca.* 100 ns).

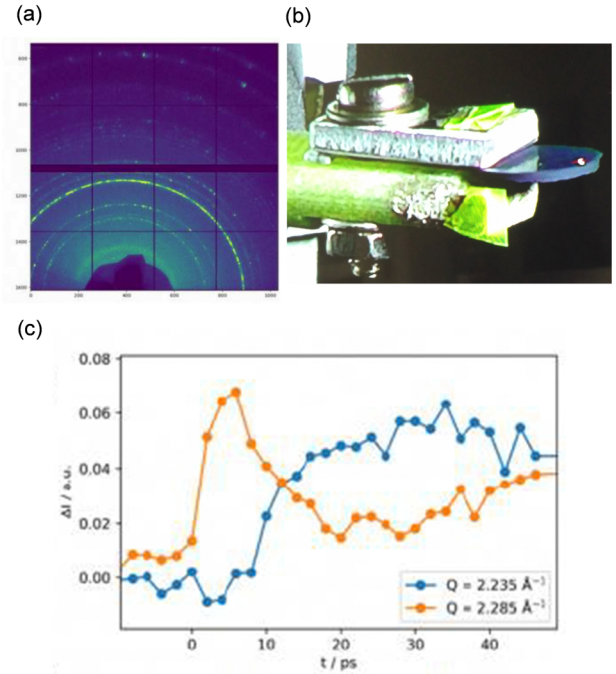

Fig. 17 (a) Debye–Scherrer ring of a sample observed using 6.6 keV photons. (b) Photograph of sample and measurement setup. (c) Lattice distortion over time. Reproduced from ref. 29, copyright 2021 Springer Nature.

Current-induced phase transition

As another stimulus, the electric current was investigated as a trigger for the phase transition.[17] A pressure-formed sample of β-Ti_3O_5 was exposed to an electric current of 0.4 A mm^{-2}, causing the brown sample to turn navy (Fig. 18(a)). The PXRD patterns prior to and following the applied electric current showed that β-Ti_3O_5 is converted into λ-Ti_3O_5 (Fig. 18(b)). The threshold current of the current-induced phase transition is 0.2 A mm^{-2}, according to the electrical current dependence of the transformation of pressure-formed β-Ti_3O_5 to λ-Ti_3O_5 (Fig. 18(c)). This current-induced phase transition likely originates from (i) the breaking of charge ordering or (ii) the Joule heat.[30–32] As shown in Fig. 6, β-Ti_3O_5 has a localized charge on Ti^{3+}(3) and an empty orbital on Ti^{4+}(2), while λ-Ti_3O_5 has a delocalized charge on Ti(2) and Ti(3). Applying an electric current to β-Ti_3O_5 impels the localized charge on Ti(3) to the vacant orbital of Ti(2), resulting in charge-delocalized λ-Ti_3O_5.

6. Summary and perspectives

This article details λ-Ti_3O_5 and a metal-substituted series called long-term heat-storage ceramics. This metal oxide can conserve the accumulated heat energy of the phase transition

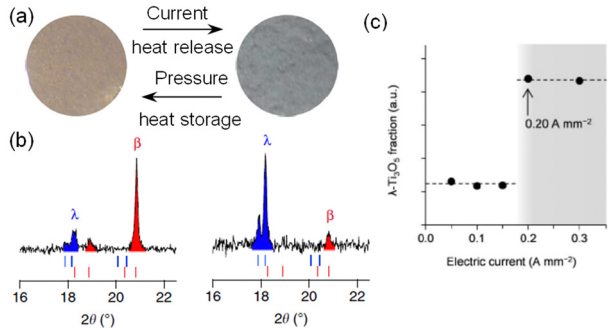

Fig. 18 (a) Color change of the sample after exposure to an electric current of 0.4 A mm^{-2}. (b) PXRD patterns before (left) and after (right) applying current. (c) Phase fraction of λ-Ti_3O_5 *vs.* electric current. Reproduced from ref. 16, copyright 2015 Springer Nature.

with β-Ti_3O_5 and release the stored energy on demand by applying external pressure. The first section provides the background that leads to the concept of long-term heat-storage ceramics. The second section explains how λ-Ti_3O_5 was first discovered and its physical properties with an emphasis on the phase transition between λ-Ti_3O_5 and β-Ti_3O_5. The third section introduces the pressure-induced phase transition from λ-Ti_3O_5 to β-Ti_3O_5 and the heat-storage property. The fourth section details approaches to control the heat-storage property. Increasing the particle size reduces the necessary pressure for heat release to 7 MPa, while substituting Ti with Mg or Sc decreases the heat-storage temperature below 100 °C. The fifth section illustrates two other features: a light-induced phase transition and a current-induced phase transition between λ-Ti_3O_5 and β-Ti_3O_5.

Such a functional metal oxide with unique heat-storage properties has potential in diverse applications (Fig. 19). For example, λ-Ti_3O_5 may be used in automobile components near engines and mufflers to rewarm cooled internal systems using the conserved waste heat upon restarting.[33,34] Additionally, this heat-storage ceramic has potential in solar power plants, which often have nitrate-based heat-storage tanks. As λ-Ti_3O_5 has both sensible and long-lasting latent heat storage, it should be a convenient alternative.[5,6,35] Furthermore, Mg-substituted λ-Ti_3O_5 or Sc-substituted λ-Ti_3O_5 with low heat-storage

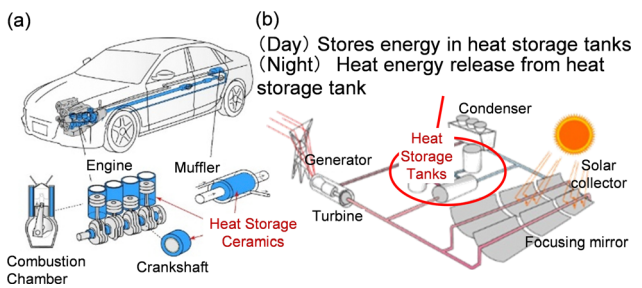

Fig. 19 Suggested applications for heat-storage ceramic λ-Ti_3O_5 in (a) internal systems of vehicles for reheating engines and (b) energy-storage tanks in solar-power systems. Reproduced from ref. 23, copyright 2019 Springer Nature.

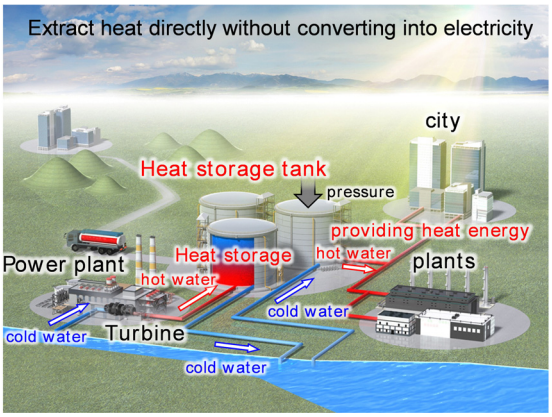

Fig. 20 Suggested application for heat-storage ceramics, Mg- and Sc-substituted λ-Ti_3O_5 for the conservation of wasted heat energy in power plants or factories. Reproduced from ref. 27, reprinted with permission from AAAS.

temperatures should be useful to reuse heat waste at power plants or factories (Fig. 20), where 70% of the generated heat energy is wasted below 100 °C.[3] Heat-storage materials functioning below the boiling point of water can recapture the thermal energy from cooling water in electric power plant turbines, which is vital to prevent rising sea-water temperatures. Moreover, the heat-storage temperature can easily be tuned by changing the Mg or Sc content in λ-Ti_3O_5 according to the target application. Such a tunable material series will expand opportunities to use thermal energy that has not been recycled.

In addition to heat-storage applications, the present material has potential in pressure-sensitive conductivity or optical sensors because λ-Ti_3O_5 is a metallic conductor while β-Ti_3O_5 is a semiconductor. Furthermore, the light-induced and current-induced phase transitions between β-Ti_3O_5 and λ-Ti_3O_5 are enticing for developing advanced electronic devices. In particular, the light-induced phase transition opens possibilities for λ-Ti_3O_5 as a candidate for next-generation superhigh-density optical storage media. The future memory density is expected to achieve one terabit $inch^{-2}$. The vast potential of λ-Ti_3O_5 has attracted many researchers: various synthesis methods have been developed,[36–49] studies of phase transition mechanism have been reported,[50–66] and novel functionalities are being explored.[67–76] Since λ-Ti_3O_5 is composed of readily available elements of titanium and oxygen, it offers harmless, sustainable, and economic features, which are advantageous in industrial applications.

One of the most important tasks for the research of λ-Ti_3O_5 material family would be the investigation of the strategy for increasing the amount of stored energy, the ΔH value between λ-Ti_3O_5 and β-Ti_3O_5. This task is of high interest not only for practical applications but also for basic science unveiling the details of the structural transformation during the phase transition. Such studies will involve theoretical calculations of the phase transition dynamics as well as highly precise time-resolved measurements and novel synthetic approaches, *i.e.*,

various aspects of basic research. The present material holds numerous directions for future research.

Conflicts of interest

There are no conflicts to declare.

Acknowledgements

This work was supported in part by a JSPS Grant-in-Aid for Scientific Research (A) (grant number 20H00369), a Japan Science and Technology FOREST Program (JPMJFR213Q), Yazaki Memorial Foundation for Science and Technology. We recognize the Cryogenic Research Center at The University of Tokyo, the Center for Nano Lithography & Analysis at The University of Tokyo, and Quantum Leap Flagship Program (Q-LEAP, grant number JPMXS0118068681) supported by MEXT.

Notes and references

1 D. Butler, *Nature*, 2007, **445**, 768–769.
2 D. Lindley, *Nature*, 2009, **458**, 138–141.
3 S. A. Rattner and S. Garimella, *Energy*, 2011, **36**, 6172–6183.
4 D. B. Gingerich and M. S. Mauter, *Environ. Sci. Technol.*, 2015, **49**, 8297–8306.
5 G. W. Crabtree and N. S. Lewis, *Phys. Today*, 2007, **60**, 37–42.
6 E. Cartlidge, *Science*, 2011, **334**, 922–924.
7 C. W. King, A. S. Holman and M. E. Webber, *Nat. Geosci.*, 2008, **1**, 283–286.
8 M. D. Bartos and M. V. Chester, *Nat. Clim. Change*, 2015, **5**, 748–752.
9 M. M. Farid, A. M. Khudhair, S. A.-K. Razack and S. Al-Hallaj, *Energy Convers. Manage.*, 2004, **45**, 1597–1615.
10 A. Sharma, V. V. Tyagi, C. R. Chen and D. Buddhi, *Renewable Sustainable Energy Rev.*, 2009, **13**, 318–345.
11 M. Barrio, D. O. López, J. L. Tamarit, P. Negrier and Y. Haget, *J. Solid State Chem.*, 1996, **124**, 29–38.
12 I. Gur, K. Sawyer and R. Prasher, *Science*, 2012, **335**, 1454–1455.
13 M. K. Nahas and F. H. Constable, *Nature*, 1938, **142**, 837.
14 K. S. Al-Jabri, A. W. Hago, A. S. Al-Nuaimi and A. H. Al-Saidy, *Cem. Concr. Res.*, 2005, **35**, 1472–1479.
15 S. Ohkoshi, Y. Tsunobuchi, T. Matsuda, K. Hashimoto, A. Namai, F. Hakoe and H. Tokoro, *Nat. Chem.*, 2010, **2**, 539–545.
16 H. Tokoro, M. Yoshikiyo, K. Imoto, A. Namai, T. Nasu, K. Nakagawa, N. Ozaki, F. Hakoe, K. Tanaka, K. Chiba, R. Makiura, K. Prassides and S. Ohkoshi, *Nat. Commun.*, 2015, **6**, 7037.
17 A. Kondo, NEDO, presented in part the 10th German-Japanese Environment and Energy Dialogue Forum, **https://www.nedo.go.jp/content/100899759.pdf**, Tokyo, October, 2019.
18 M. Onoda, *J. Solid State Chem.*, 1998, **136**, 67–73.
19 T. Nasu, H. Tokoro, K. Tanaka, F. Hakoe, A. Namai and S. Ohkoshi, *Mater. Sci. Eng.*, 2014, **54**, 012008.
20 Y. Araki, S. Ohkoshi and H. Tokoro, *Mater. Today Energy*, 2020, **18**, 100525.
21 W. H. Zachariasen, *J. Less-Common Met.*, 1978, **62**, 1–7.
22 C. P. Slichter and H. G. Drickamer, *J. Chem. Phys.*, 1972, **56**, 2142–2160.
23 S. Ohkoshi, H. Tokoro, K. Nakagawa, M. Yoshikiyo, F. Jia and A. Namai, *Sci. Rep.*, 2019, **9**, 13203.
24 S. Ohkoshi, Y. Maeno and T. Nasu, *International Pat.*, WO2017/164083, 2017.
25 M. Wang, W. Huang, Z. Shen, J. Gao, Y. Shi, T. Lu and Q. Shi, *J. Alloys Compd.*, 2019, **774**, 1189–1194.
26 S. Ohkoshi, F. Jia, M. Yoshikiyo, K. Imoto, H. Tokoro, K. Nakagawa, Y. Maeno, A. Namai, R. Harada, K. Hattori, K. Kojima, K. Sugiura and T. Suganuma, *Mater. Adv.*, 2022, **3**, 4824–4830.
27 Y. Nakamura, Y. Sakai, M. Azuma and S. Ohkoshi, *Sci. Adv.*, 2020, **6**, 5264.
28 H. Tokoro, A. Namai, M. Yoshikiyo, K. Chiba, R. Fujiwara and S. Ohkoshi, *Sci. Rep.*, 2018, **8**, 63.
29 C. Mariette, M. Lorenc, H. Cailleau, E. Collet, L. Guérin, A. Volte, E. Trzop, R. Bertoni, X. Dong, B. Lépine, O. Hernandez, E. Janod, L. Cario, V. Ta Phuoc, S. Ohkoshi, H. Tokoro, L. Patthey, A. Babic, I. Usov, D. Ozerov, L. Sala, S. Ebner, P. Böhler, A. Keller, A. Oggenfuss, T. Zmofing, S. Redford, S. Vetter, R. Follath, P. Juranic, A. Schreiber, P. Beaud, V. Esposito, Y. Deng, G. Ingold, M. Chergui, G. F. Mancini, R. Mankowsky, C. Svetina, S. Zerdane, A. Mozzanica, A. Bosak, M. Wulff, M. Levantino, H. Lemke and M. Cammarata, *Nat. Commun.*, 2021, **12**, 1239.
30 S. Ikeda, K. Miura, H. Yamamoto, K. Mizunuma, H. D. Gan, M. Endo, S. Kanai, J. Hayakawa, F. Matsukura and H. Ohno, *Nat. Mater.*, 2010, **9**, 721–724.
31 A. Asamitsu, Y. Tomioka, H. Kuwahara and Y. Tokura, *Nature*, 1997, **388**, 50–52.
32 M. Yamanouchi, D. Chiba, F. Matsukura and H. Ohno, *Nature*, 2004, **428**, 539–542.
33 A. Honda and S. Ohkoshi, *JP Pat.*, JP6426658, 2018.
34 A. Honda and S. Ohkoshi, *DE Pat.*, DE102017109005, 2018.
35 S. Garimella, K. Lockyear, D. Pharis, O. El Chawa, M. T. Hughes and G. Kini, *Joule*, 2022, **6**, 956–971.
36 G. Liu, W. X. Huang and Y. Yi, *J. Inorg. Mater.*, 2013, **28**, 425–430.
37 Y. Chen and J. Mao, *J. Mater. Sci.: Mater. Electron.*, 2014, **25**, 1284–1288.
38 N. Stem, M. L. de Souza, D. L. A. de Faria and S. G. dos Santos Filho, *Thin Solid Films*, 2014, **558**, 67–74.
39 G. Chai, W. Huang, Q. Shi, S. Zheng and D. Wei, *J. Alloys Compd.*, 2015, **621**, 404–410.
40 D. Wei, W. Huang, Q. Shi, T. Lu and B. Huang, *J. Mater. Sci.: Mater. Electron.*, 2016, **27**, 4216–4222.
41 Z. Shen, Q. Shi, W. Huang, B. Huang, M. Wang, J. Gao, Y. Shi and T. Lu, *Appl. Phys. Lett.*, 2017, **111**, 191902.
42 L. Wang, X. Zhang, W. Liu, W. Xu, A. Singh and Y. Lin, *J. Mater. Sci.: Mater. Electron.*, 2017, **28**, 6421–6425.
43 W. Qi, J. Du, Y. Peng, Y. Wang, Y. Xu, X. Li, K. Zhang, C. Gong, M. Luo and H. Peng, *Vacuum*, 2017, **143**, 380–385.
44 Z. Ertekin, N. Ö. Pekmez and K. Pekmez, *J. Solid State Electrochem.*, 2020, **24**, 975–986.
45 H. Chen, Y. Hirose, K. Nakagawa, K. Imoto, S. Ohkoshi and T. Hasegawa, *Appl. Phys. Lett.*, 2020, **116**, 201904.
46 Y. Cai, Q. Shi, M. Wang, X. Lv, Y. Cheng and W. Huang, *J. Alloys Compd.*, 2020, **848**, 156585.
47 P. Sun, X. Hu, G. Wei, R. Wang, Q. Wang, H. Wang and X. Wang, *Appl. Surf. Sci.*, 2021, **548**, 149269.
48 P. Zhao, G. Li, W. Li, P. Cheng, Z. Pang, X. Xiong, X. Zou, Q. Xu and X. Lu, *Trans. Nonferrous Met. Soc. China*, 2021, **31**, 3310–3327.
49 K. Yoshimatsu and H. Kumigashira, *Cryst. Growth Des.*, 2022, **22**, 703–710.
50 R. Liu and J.-X. Shang, *Modell. Simul. Mater. Sci. Eng.*, 2012, **20**, 035020.
51 R. Liu, J.-X. Shang and F.-H. Wang, *Comput. Mater. Sci.*, 2014, **81**, 158–162.
52 A. Asahara, H. Watanabe, H. Tokoro, S. Ohkoshi and T. Suemoto, *Phys. Rev. B: Condens. Matter Mater. Phys.*, 2014, **90**, 014303.
53 A. Ould-Hamouda, H. Tokoro, S. Ohkoshi and E. Freysz, *Chem. Phys. Lett.*, 2014, **608**, 106–112.
54 D. Olguín, E. Vallej and A. Rubio-Ponce, *Phys. Status Solidi B*, 2015, **252**, 659–662.
55 E. Vallejo and D. Olguín, *Mater. Res. Express*, 2015, **2**, 126101.
56 F. Hakoe, H. Tokoro and S. Ohkoshi, *Mater. Lett.*, 2017, **188**, 8–12.
57 K. Kobayashi, M. Taguchi, M. Kobata, K. Tanaka, H. Tokoro, H. Daimon, T. Okane, H. Yamagami, E. Ikenaga and S. Ohkoshi, *Phys. Rev. B*, 2017, **95**, 085133.
58 K. R. Tasca, V. Esposito, G. Lantz, P. Beaud, M. Kubli, M. Savoini, C. Giles and S. L. Johnson, *ChemPhysChem*, 2017, **18**, 1385–1392.
59 X.-K. Fu, W.-Q. Chen, Z.-S. Jiang, B. Yang, X. Zhao and L. Zuo, *Acta Phys. Sin.*, 2019, **68**, 207301.
60 X.-K. Fu, B. Yang, W.-Q. Chen, Z.-S. Jiang, Z.-B. Li, H.-L. Yan, X. Zhao and L. Zuo, *Comput. Mater. Sci.*, 2020, **173**, 109435.
61 X. Fu, X. Hao, W. Chen, B. Yang, X. Zhao and L. Zuo, *J. Phys.: Condens. Matter*, 2020, **32**, 46LT01.
62 S. V. Hosseini, M. Abbasnejad and M. R. Mohammadizadeh, *Phys. Rev. B*, 2021, **104**, 224101.
63 T. Takeda and S. Ohkoshi, *Eur. J. Inorg. Chem.*, 2022, e202101037.
64 T. Saiki, T. Yoshida, K. Akimoto, D. Indo, M. Arizono, T. Okuda and T. Katsufuji, *Phys. Rev. B*, 2022, **105**, 075134.

65 D. Peng, N. Jin, Y. Liu, T. Yuan, P. Xiao and J. Ye, *Mater. Today Commun.*, 2022, **31**, 103332.
66 S. Jütten and T. Bredow, *J. Phys. Chem. C*, 2022, **126**, 7809–7817.
67 A. Kitada, G. Hasegawa, Y. Kobayashi, K. Kanamori, K. Nakanishi and H. Kageyama, *J. Am. Chem. Soc.*, 2012, **134**, 10894–10898.
68 G. Hasegawa, T. Sato, K. Kanamori, K. Nakano, T. Yajima, Y. Kobayashi, H. Kageyama, T. Abe and K. Nakanishi, *Chem. Mater.*, 2013, **25**, 3504–3512.
69 Z. Ertekin, U. Tamer and K. Pekmez, *Electrochim. Acta*, 2015, **163**, 77–81.
70 Q. Shi, G. Chai, W. Huang, Y. Shi, B. Huang, D. Wei, J. Qi, F. Su, W. Xu and T. Lu, *J. Mater. Chem. C*, 2016, **4**, 10279–10285.
71 X. Zhang, W. Liu, H. Yu, X. Zhong, L. Wang, A. Singh and Y. Lin, *Micro Nano Lett.*, 2016, **11**, 811–813.
72 R. Alipour Moghadam Esfahani, S. K. Vankova, A. H. A. Monteverde Videla and S. Specchia, *Appl. Catal., B*, 2017, **201**, 419–429.
73 R. Takahama, T. Ishii, D. Indo, M. Arizono, C. Terakura, Y. Tokura, N. Takeshita, M. Noda, H. Kuwahara, T. Saiki, T. Katsufuji, R. Kajimoto and T. Okuda, *Phys. Rev. Mater.*, 2020, **4**, 074401.
74 X. Fu, W. Chen, X. Hao, Z. Zhang, R. Tang, B. Yang, X. Zhao and L. Zuo, *J. Mater. Chem. C*, 2021, **9**, 7976–7981.
75 E. Widyastuti, F.-Y. Xu, C.-T. Chiu, J.-H. Jan, J.-L. Hsu and Y.-C. Lee, *Catalysts*, 2021, **11**, 1416.
76 S. Zhang, Y. Zhang, Y. Huang, B. Lin, S. Ling, C. Mei and M. Pan, *Chem. Eng. J.*, 2022, **450**, 137910.

